






# Modeling the electrical characteristics of InGaN/GaN LED structures based on experimentally-measured defect characteristics

Nicola Roccato<sup>1</sup> , Francesco Piva<sup>1</sup> , Carlo De Santi<sup>1</sup>, Riccardo Brescancin<sup>1</sup>, Kalparupa Mukherjee<sup>1</sup>, Matteo Buffolo<sup>1</sup>, Camille Haller<sup>2</sup>, Jean-François Carlin<sup>2</sup>, Nicolas Grandjean<sup>2</sup>, Marco Vallone<sup>3</sup> , Alberto Tibaldi<sup>3</sup> , Francesco Bertazzi<sup>3</sup>, Michele Goano<sup>3</sup>, Giovanni Verzellesi<sup>4</sup>, Gaudenzio Meneghesso<sup>1</sup> , Enrico Zanoni<sup>1</sup> and Matteo Meneghini<sup>1</sup>

<sup>1</sup> Dipartimento di Ingegneria dell'Informazione, Università di Padova, via Gradenigo 6/B, Padova 35131, Italy

<sup>2</sup> Institute of Physics, School of Basic Sciences, Ecole Polytechnique fédérale de Lausanne (EPFL), CH-1015 Lausanne, Switzerland

<sup>3</sup> Politecnico di Torino, Corso Duca degli Abruzzi, 24, 10129 Torino, Italy

<sup>4</sup> Dipartimento di Scienze e Metodi dell'Ingegneria and Centro En&tech, Università di Modena e Reggio Emilia, via Amendola 2, Pad. Morselli, 42122 Reggio Emilia, Italy

E-mail: [roccatonic@dei.unipd.it](mailto:roccatonic@dei.unipd.it)

Received 19 March 2021, revised 14 July 2021

Accepted for publication 22 July 2021

Published 4 August 2021



## Abstract

Defects can significantly modify the electro-optical characteristics of InGaN light-emitting diodes (LEDs); however, modeling the impact of defects on the electrical characteristics of LEDs is not straightforward. In this paper, we present an extensive investigation and modeling of the impact of defects on the electrical characteristics of InGaN-based LEDs, as a function of the thickness of the quantum well (QW). First, we demonstrate that the density of defects in the active region of III-N LEDs scales with increasing thickness of the InGaN QW. Since device layers with high indium content tend to incorporate more defects, we ascribed this experimental evidence to the increased volume of defects-rich InGaN associated to thicker InGaN layers. Second, we demonstrate that the current–voltage characteristics of the devices are significantly influenced by the presence of defects, especially in the sub turn-on region. Specifically, we show that the electrical characteristics can be effectively modeled in a wide current range (from pA to mA), by considering the existence of trap-assisted tunneling processes. A good correspondence is obtained between the experimental and simulated electrical characteristics ( $I$ – $V$ ), by using—in the simulation—the actual defect concentrations/activation energies extracted from steady-state photocapacitance, instead of generic fitting parameters.

**Keywords:** light-emitting diodes, InGaN/GaN, deep defects, simulation, tunneling, Trap-assisted tunneling

(Some figures may appear in colour only in the online journal)

## 1. Introduction

The deep defects present in light-emitting diodes (LEDs), particularly in the active region (AR), can significantly impact on the optical and electrical characteristics of the devices. With regard to the optical properties, deep traps may behave as Shockley–Read–Hall (SRH) recombination centers, and decrease the efficiency of the devices, especially at low current levels, where SRH recombination plays the strongest role. Recent papers [1–3] demonstrated that the efficiency of InGaN LEDs is strongly influenced by the presence of midgap states, located in the quantum well (QW) region, that can favor SRH recombination.

With regard to the electrical properties, the relation is less straightforward. Recently, it has been proposed that deep traps located in the depleted region can favor trap-assisted tunneling (TAT) of carriers, thus significantly increasing the sub turn-on leakage current [4–6]. Understanding and modeling the current–voltage characteristics of LEDs in a wide current range (from pA to 10–100 mA) is a fundamental step to identify specific non-idealities related to the presence of defects, that lead to an increase in the leakage current, especially below the turn-on voltage of the diode (typically around 3.2–3.5 V) [6]. In addition, by observing the sub turn-on voltage electrical characteristics during an ageing experiment, it is possible to identify specific degradation processes (such as defect generation and/or diffusion), and improve consequently the epitaxy [7–9].

However, modeling the current–voltage characteristics of LEDs in a wide range of currents is not trivial, since many mechanisms can contribute to leakage current conduction. Previous papers [10–12] preliminarily explored this topic, mainly based on the comparison between experimental current–voltage ( $I$ – $V$ ) characteristics and simulations. However, the simulations were based on hypothetical defect parameters, rather than on actual data obtained from defect characterization, and the models could not be validated against actual defect concentrations/activation energies.

This paper makes a step forward in this field, demonstrating that the defect characterization data obtained through steady-state photocapacitance (SSPC) can be effectively used to reproduce with great accuracy the current–voltage characteristics of InGaN LEDs with different density of defects in the AR, in a wide current range (over several orders of magnitude, from pA to 100 mA).

The approach to the study is based on two steps. In the first step, we fabricated and characterized three different LED wafers, having different densities of defects incorporated in the (single) InGaN QWs. The properties of these defects (ionization energy, density, ...) were estimated by SSPC measurements: we demonstrated that the density of defects in the AR of the devices (composed of barriers and QWs) increases with increasing thickness of the single QW. This result indicates that defects are preferentially incorporated in indium-containing layers, confirming previous studies on the topic [13–16].

In the second step, we defined a model for the current–voltage characteristics of InGaN QW-based diodes,

considering TAT as the main leakage mechanisms, using as a starting point the considerations proposed in early studies on the topic [10–12]. After model calibration, and verification of the sensitivity to the main parameters, the parameters of traps extracted in the first step were fed into the model, to reproduce the electrical characteristics of the devices. A good matching with the current–voltage characteristics of the diodes was found over more than 10 order of magnitude in current. The results demonstrate that a calibration of the electrical model against experimentally-validated defect-properties is the key step for accurately reproducing the current–voltage characteristics of LEDs.

## 2. Samples and methodology

The devices analyzed within this paper are InGaN/GaN LEDs, that were grown on a sapphire substrate (figure 1), having an area of  $300 \times 300 \mu\text{m}^2$ . The epitaxial structure consists of a 800 nm n-doped GaN buffer with  $N_D = 3 \times 10^{18} \text{ cm}^{-3}$ , followed by a super lattice under layer (SL UL) constituted by 24 layers of  $\text{Al}_{0.17}\text{In}_{0.83}\text{N}/\text{GaN}$  (2.1 nm/1.7 nm). The first 22 layers have a doping concentration equal to  $N_D = 3 \times 10^{18} \text{ cm}^{-3}$ , while the last two ones are over-doped at  $1 \times 10^{20} \text{ cm}^{-3}$ . The function of the UL is to incorporate the defects coming from the GaN buffer layer [1], in order to guarantee a lower concentration of traps in the AR and therefore a better efficiency of the device [12–15]. The AR of the device consists of an undoped single QW, placed between two 7.5 nm barriers ( $N_D = 3 \times 10^{18} \text{ cm}^{-3}$ ) and two spacers. After the undoped spacer, a p-doped  $\text{Al}_{0.06}\text{Ga}_{0.94}\text{N}$  layer was used as electron blocking layer (EBL) with  $N_A = 5 \times 10^{18} \text{ cm}^{-3}$ , followed by a p-doped 180 nm GaN layer with the same doping concentration. The anode contact is made by an alloy of gold and platinum, which is placed on a p-doped 20 nm GaN layer with  $N_A = 2 \times 10^{19} \text{ cm}^{-3}$ .

Three different wafers were used, having exactly the same structure, but different thickness of the QW. Due to the different structures, the analyzed samples were found to have different defect densities in the active layer, thus being ideal to validate our model (see results in the next sections). Specific properties of the SQW for the three wafers are: indium content = 20%; thicknesses equal to 1.3 nm, 1.8 nm and 2.4 nm, respectively, for the wafers named A, B and C.

A first electrical characterization was carried out by voltage current measurements ( $I$ – $V$ ). Then, in order to study the activation energy and density of deep defects, we adopted SSPC and light-dark capacitance-voltage (LCV) measurements. Finally, numerical simulation were carried out with the TCAD Sentaurus suite from Synopsys Inc. [17, 18], to reproduce the electrical characteristics, with particular focus on how the defects affect the electrical behavior of the devices.

## 3. Analysis of experimental data

To identify the presence of defects within the AR of the analyzed devices, two different techniques were used: SSPC, to



**Figure 1.** Diagram of the structure of the LED devices analyzed within this paper. Three identical wafers, differing only for the thickness of the quantum well, were fabricated. The properties of the quantum well are: indium content = 20%; thicknesses equal to 1.3 nm, 1.8 nm and 2.4 nm respectively for the wafers named A, B and C.

identify the ionization energy of the defects, and LCV measurements, to quantify the density of the defects.

### 3.1. Ionization energy of the defects

SSPC determines the energy level of a defect state from the photo-capacitance response due to deep level photoemission. To perform this analysis, the samples were exposed to sub-band gap, monochromatic illumination. The measurements were conducted at room temperature at 1 MHz and the AC-signal amplitude was equal to 50 mV. A custom system consisting of a mercury lamp, a monochromator, a focusing lens and an optical fiber provided monochromatic excitation in the photon energy range between 1.1 eV and 3.5 eV. The photon flux ( $\phi$ ) varied between  $-1 - 25 \times 10^{17} \text{ cm}^{-2} \text{ s}^{-1}$ . The bias voltage applied to the device was  $V = 0 \text{ V}$  and it was chosen to ensure that the space charge region (SCR) was wide enough to include the AR. In fact from the capacitance-voltage (CV) in dark condition we can determine a depletion depth ( $x_d$ ) of about 46 nm at 0 V, indicating that the SCR extends from the end of the EBL to the start of the SL UL as reported in figure 2.

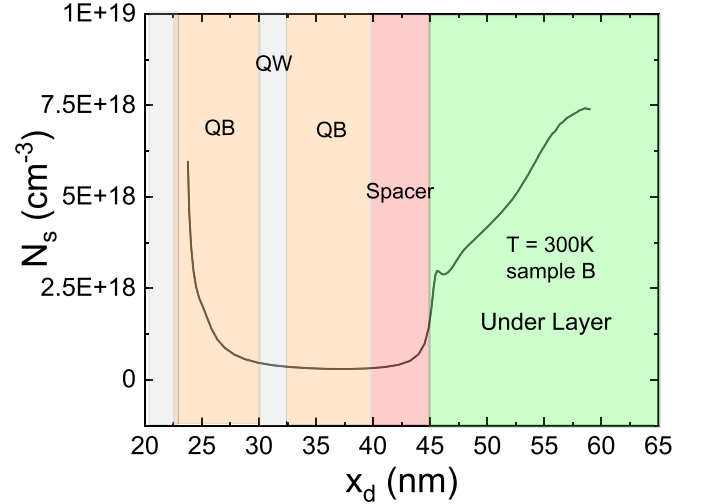


**Figure 2.** Apparent charge profile, as obtained from the CV measurements [13]. The various regions of the device are highlighted for clarity. The peak at charge at about 46 nm is associated to the interface between the under layer and the over-doped spacer. Thus, the region analyzed by SSPC measurements include the layers located above this interface (Spacers, QBs and QW).

Thus, all analysis in the following aims at estimating the properties of traps located in the AR [19–21]. In the following discussion, ‘active region’ is defined as the ensemble of the QW and the two surrounding barriers and spacers (see details below).

From the ratio between the time derivative of the photo-capacitance transient at  $t = 0 \text{ s}$  and the photon flux  $\phi$ , it is possible to obtain the deep level photoionization cross-section (PCS) of the traps (see figure 3). The PCS curves were fitted by using the model proposed by Passler *et al* [22]:

$$\sigma(h\nu, T) \simeq \frac{\text{const.}}{h\nu \sqrt{2\pi d_{\text{FC}} \epsilon \coth\left(\frac{E_{\text{ph}}}{2k_B T}\right)}} \times \int_0^{(+\infty)} dE_k \frac{E_p^{\frac{3}{2}}}{(E_p + E^O - d_{\text{FC}})^2} \times \exp\left[-\frac{(h\nu - E^O - E_p)^2}{2D \epsilon \coth\left(\frac{E_{\text{ph}}}{2k_B T}\right)}\right] \quad (1)$$

that takes into account the lattice relaxation of the deep level defect having given optical ionization energy ( $E^O$ ) and Franck-Condon shift ( $d_{\text{FC}}$ ). It is worth mentioning that the thermal ionization energy  $E_T$  (also referred to as electron binding energy) can be calculated from the optical ionization energy as  $E_T = E^O - d_{\text{FC}}$ ; also,  $E_p = h\nu - E_T$  is the energy of the excited electron and  $E_{\text{ph}} = h\nu$  the effective phonon energy.

From this analysis, we obtained an estimation of the optical ionization energy of the deep defects of the three LEDs. In figure 3 representative PCS data are reported, indicated by symbols; the solid lines represent the fits

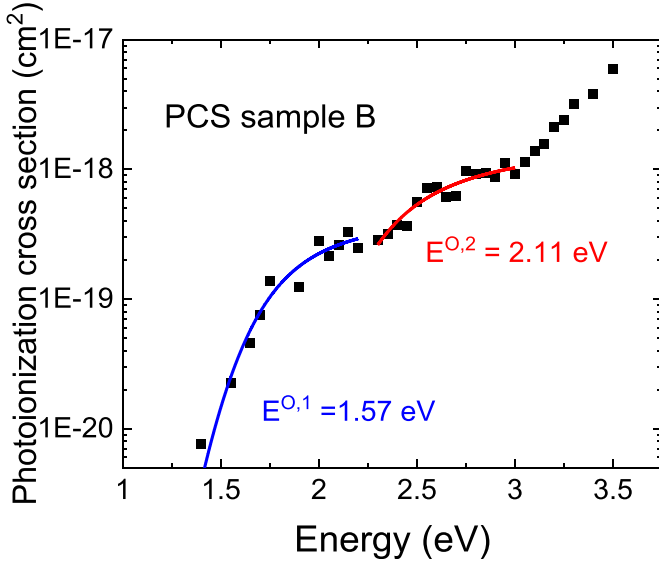


**Figure 3.** Example of extraction of energy levels of traps using PCS on a representative device. The symbols represent the photoionization cross section, measured as a function of photon energy. The blue and red lines the fits to the Passler model for respectively the first and the second energy level. Two levels can be clearly identified.

**Table 1.** Energy levels of defects for the three analyzed wafers, as obtained from deep-level optical spectroscopy measurements.

Sample	A (1.3 nm)	B (1.8 nm)	C (2.4 nm)
$E^{0,1}$ level 1 (eV)	1.66	1.57	1.66
$E^{0,2}$ level 2 (eV)	2.1	2.11	2.07
$E_C - E_{T,1}$ , level 1 (eV)	1.29	1.28	1.29
$E_C - E_{T,2}$ , level 2 (eV)	1.71	1.72	1.67

according to the Passler model: two defect-related edges are observed, one near midgap ( $E^{0,2} = 2.11$  eV, corresponding to  $E_C - E_{T,2} = 1.72$  eV, where  $E_C$  is the conduction band energy), the other corresponding to a less deep defect ( $E^{0,1} = 1.57$  eV, corresponding to  $E_C - E_{T,1} = 1.28$  eV). The change in slope above 3 eV does not correspond to a deep level, but to the generation of carriers within the QW.

The results obtained on the three wafers analyzed are summarized in table 1, that reports the energies extrapolated for each of the absorption edges. As can be noticed, the three wafers showed the presence of the same two deep levels, one with energy in the range 1.28–1.29 eV below the conduction band energy, the other with energy in the range 1.67–1.72 eV below the conduction band energy.

### 3.2. Analysis of the density of the defects

As discussed in the previous section, the same set of two defects was found in all analyzed samples. What differs for the three wafers is the concentration of the defects. To quantitatively evaluate the trap density of the two levels identified, Light-Dark CV measurements were carried out. The measurement procedure consists of two CV measurements, one in dark

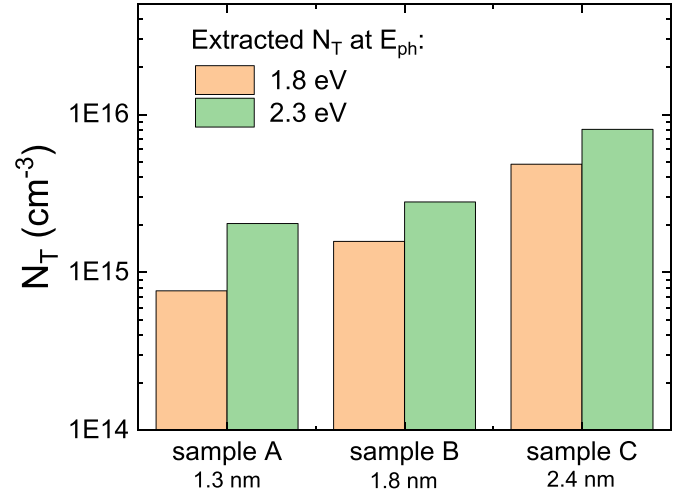


**Figure 4.** Estimation of the average trap concentration until 1.8 eV and 2.3 eV from the conduction band in the active region (i.e. SQW and the surrounding barriers and spacers) obtained by the light-dark CV measurements.

conditions and one under monochromatic light. The excitation wavelength is chosen in order to selectively excite each of the defects identified by SSPC.

The variation in space-charge density due to deep level photoemission under monochromatic, sub-bandgap illumination is then measured. LCV was performed at 1 MHz; it is worth noticing that during our measurements the phase of the impedance of the devices was always between  $-85^\circ$  and  $-90^\circ$ , indicating that device is effectively behaving as a capacitor, with extremely high parallel resistance (negligible parallel leakage). The absence of leakage-related issues results in a reliable capacitance reading in the whole analyzed range.

The estimation of the concentration of traps was carried out with the same procedure used by Armstrong [19–21] where the additional voltage  $\Delta V$  required to reach  $x_d$  when defects are emptied by illumination compared to when the defects are fully occupied is:

$$\Delta V = \frac{q}{\epsilon} \int_0^{x_{\{d\}}} x N_T dx. \quad (2)$$

Here  $q$  is the elementary charge,  $\epsilon$  the semiconductor permittivity and the trap concentration  $N_T$  is approximated constant in the (narrow) AR.

The measurement was repeated for two different photon energies. To determine the concentration of traps of the first energy level, the photon energy was set at 1.8 eV, so as to optically stimulate only the  $E^{0,1} \sim 1.66$  eV level. For stimulating also the second trap energy level ( $E^{0,2} \sim 2.11$  eV), the photon energy was set at 2.3 eV. By subtracting the 1.8 eV concentration from that obtained at 2.3 eV, we obtain an estimate of the concentration of the second energy level.

In figure 4 and in table 2 a summary of the results is reported. The bar plot reports the average trap density in the AR, i.e. the region including the SQW and the surrounding barriers. It is worth noticing that due to the spatial resolution of



**Table 2.** Trap concentration at the identified energy levels. The concentration at the first level is estimated by setting the photon energy at 1.8 eV, while the concentration of the second level is given by the difference between the estimate obtained at 2.3 eV and the one at 1.8 eV.

sample	A (1.3 nm)	B (1.8 nm)	C (2.4 nm)
conc. level 1 ( $\text{cm}^{-3}$ )	7.66E14	1.57E15	4.85E15
conc. level 2 ( $\text{cm}^{-3}$ )	1.27E15	1.23E15	3.21E15

the measurements, it is impossible to selectively measure just the QW.

First, a monotonic dependence of trap concentration on the QW width can be observed. In fact, with increasing the QW width, the average concentration of defects in the AR increases. Previous papers [13–16] indicated that, during growth, defects are typically incorporated in In-containing layers, and this is consistent with our experimental results. In addition to that, the presence of thicker InGaN QW may impact on the epitaxial strain within the adjacent GaN layers, thus contributing to further increase the defectiveness of these semiconductor regions [3, 23–25]. Therefore, we can reasonably assume that the detected increase in average  $N_T$  is representative of an increased defect concentration within the QW (related to indium incorporation [13–16] and mostly impacting the recombination efficiency), and the semiconductor layers close to the AR of the device (spacers + barriers + QW, mostly impacting the electrical characteristics). Since the defect densities reported in figure 4 are related to the AR, and the total thickness of the investigated AR is identical for all wafers, we conclude that an increased thickness of the QW results in a higher density of defects.

Second, from the SSPC and Light-Dark CV measurements, the energy levels and concentration of the deep levels were obtained: the results are summarized in table 2. These results were used to build the model for simulating the electrical characteristics of the devices, as described in the next sections.

## 4. Modeling

Numerical simulations were carried out with the TCAD Sentaurus suite from Synopsys Inc. The structure has been reproduced by the SDE tool, and the layers have been doped by placing the traps (Si and Mg) at the characteristic energy levels as indicated in table 3 [26–29]. In the simulations, SRH, radiative and Auger generation–recombination mechanisms, and thermionic emission processes were considered. The main material parameters for these mechanisms in binary and ternary compounds have been used, as reported in table 3.

### 4.1. Parasitic resistances

The first step in the calibration of the TCAD model was the extraction of the series and parallel (shunt) resistance of the devices. In order to simulate the current leakage due to parasitic paths, that act in the electrical characteristic at low voltages (near 0 V) a parallel resistance ( $R_p$ ) has been

**Table 3.** Most relevant material parameters.

	GaN	AlGaIn	InGaIn	AlInN
x content	—	6%	20%	17%
SRH lifetime (s)	5E-8	5E-8	5E-8	5E-8
B ( $\text{cm}^3\text{s}^{-1}$ )	2E-10	1.9E-10	2E-10	1.72E-10
C ( $\text{cm}^6\text{s}^{-1}$ )	1E-30	1E-30	1E-30	1E-30
Donor activation energy (meV)	20	—	—	150
Acceptor activation energy (meV)	150	200	—	—

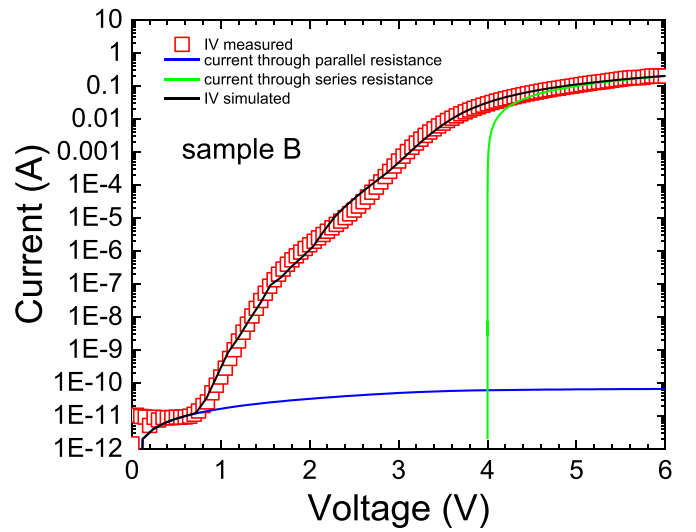


**Figure 5.** Comparison among the experimental IV (red line), the simulated IV with parasitic resistances implemented (black line), and the current through the parallel parasitic resistor (violet) and the resistive behavior due to the series one (green). The parallel parasitic resistance act in the electrical characteristic at low voltages while the series one at voltages over the turn on voltage.

added to the device. The chosen value is  $6 \times 10^{10} \Omega$  for all the three LEDs, as extrapolated from the current–voltage characteristics. With regard to the series resistance ( $R_s$ ), that may originate from non-ideal contacts, buffer layers, partial activation of doping, etc [30], the value was been calibrated to reach a matching of the slope of the linear  $I$ – $V$  plot at high voltages, and is around  $10 \Omega$ . In figure 5 the effects of parasitic resistances in the IV can be observed, along with the measured  $I$ – $V$  plot and the final  $I$ – $V$  simulated characteristics.

### 4.2. Anode contact

The p contact is made of platinum with a work function of 6.35 eV ( $\Phi_M$ ) [31], and which forms a Schottky contact. The quality of the ohmic contact has a strong impact on charge injection of the device, and on the final parasitic resistance. The charge injection was modeled by considering thermionic emission and tunneling. At present, tunneling is believed to be the primary mechanism for low resistivity contacts, since the barrier for thermionic emission is relatively high at the metal/p–GaN interface. Tunneling contacts are typically based

on highly-doped material (see the device cross section in figure 1). This thin layer allows to regulate through doping, and therefore through the thickness of the potential barrier  $\Phi_{BE}$ , the efficiency with which tunneling takes place. The resistivity due to tunneling is in fact given by [32]:

$$\rho = \frac{k}{\pi q A^* T} \sin(\pi c_1 k T) \exp\left(\frac{q \Phi_{BE}}{E_{00}}\right) \quad (3)$$

where  $E_{00}$  is a tunneling parameter, and  $c_1$  depend on the position of the Fermi level,  $E_{00}$  and  $\Phi_{BE}$ . For lower barriers  $\Phi_{BH}$ , there is a lower resistivity and thus a higher charge injection efficiency. By adjusting the doping of the thin layer and the contact work function  $\Phi_M$ , it is therefore possible to control the charge injection which has the primary effect of changing the threshold voltage of the device.

#### 4.3. Tunneling model

The main mechanism responsible for sub turn-on leakage is TAT. This phenomenon influences the IV characteristics below the turn-on voltage. It is determined by electrons and holes tunneling from respectively the n-type side and the p-type side, towards defect states located mainly within the forbidden bandgap of the undoped spacer (figure 6).

Tunneling charges occupy the trap states and then recombine non-radiatively. So, the traps act as efficient non radiative recombination centers. The model implemented for describing tunneling to traps considers the combination of two capture/emission mechanisms, a phonon-assisted inelastic process, and an elastic transition [12, 17, 33, 34]. The electron capture rate for the phonon-assisted transition from the conduction band is:

$$c_n^{\text{phon}} = \frac{2V_r S \omega \sqrt{m_t(m_0 k_B T)^3}}{\hbar \sqrt{\chi}} \left( \frac{(S-l)^2}{S} \right) \times \exp\left[-S(2f+1) + \frac{\Delta E}{2k_B T + \chi}\right] \left( \frac{\gamma}{l + \chi} \right)^l \times F_{\frac{1}{2}}\left[\frac{E_{F,n} - E_C(0)}{k_B T}\right] \frac{|\Psi(z_0)|^2}{|\Psi(0)|^2} \quad (4)$$

while the electron capture rate for the elastic transition from the conduction band is:

$$c_n^{\text{el}} = \frac{2V_r S \theta \sqrt{8m_t m_0^{\frac{3}{2}}}}{\hbar^4 \pi} (E_C(z_0) - E_T)^2 (E_T - E_C(0))^{\frac{3}{2}} \times F_{\frac{1}{2}}\left[\frac{E_{F,n} - E_T}{k_B T}\right] \frac{|\Psi(z_0)|^2}{|\Psi(0)|^2} \quad (5)$$

where  $E_T$  is the energy level of the traps referred to the intrinsic Fermi level ( $E_T = E_t - E_i$ ),  $V_T$  is the interaction volume of the trap,  $S$  is the Huang-Rhys factor,  $\hbar\omega$  the energy of the phonons involved in the transition ( $E_{\text{phon}}$ ),  $m_t$  is the tunneling electron effective mass,  $l$  is the number of the phonons emitted in the transition,  $f$  is the Bose-Einstein occupation of the phonon state and finally,  $z = 2S\sqrt{f(f+1)}$  and  $\chi = \sqrt{l^2 + z^2}$ . The dissipated energy in this process is  $\Delta E = E_C + \frac{3}{2}k_B T - E_T$ .

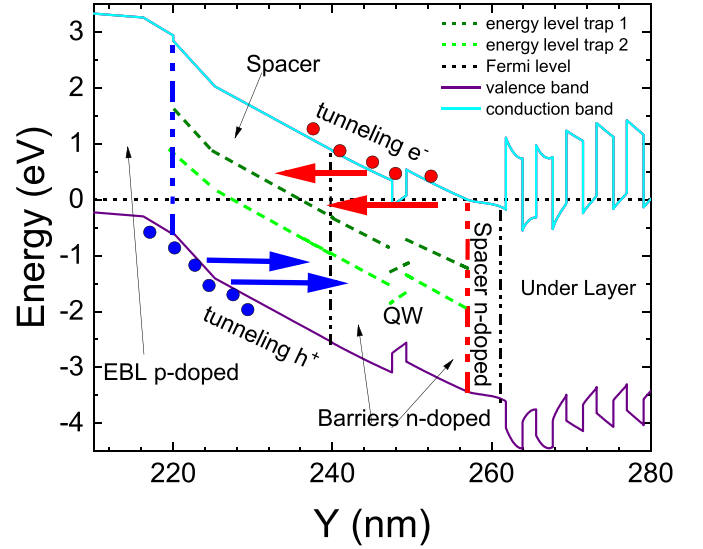


**Figure 6.** Trap assisted tunneling mechanisms implemented in the model. Electrons and holes tunnel into trap states located near the midgap of the forbidden band of the undoped GaN spacer from the n-region; there they recombine non radiatively causing the forward TAT current. (The representation of tunneling is simplified. In fact, the arrival energy at the end of the tunneling  $E_{\text{opt}}$  is in general different from the trap energy. In particular,  $E_{\text{opt}}$  is the energy that maximizes the product between tunneling probability and capture probability.).

This model for TAT works as an additional SRH recombination rate:

$$R_{\text{TAT}} = \frac{N_T c_n c_p (np - n_i^2)}{c_n \left( n + \frac{n_i}{g_n} e^{\frac{E_T}{k_B T}} \right) + c_p \left( p + \frac{n_i}{g_p} e^{-\frac{E_T}{k_B T}} \right)} \quad (6)$$

where  $N_T$  is the trap density,  $g_{n,p}$  are the electron and hole degeneracy factors and  $c_{n,p}$  are the capture rates described above.

In the simulations we have set  $S = 10$ ,  $V_T = 2 \times 10^{-7} \mu\text{m}^3$ ,  $E_{\text{phon}} = 91.2 \text{ meV}$ , the electron and hole cross-section of the trap  $\sigma_e = 1 \times 10^{-11} \text{ cm}^2$  and  $\sigma_h = 1 \times 10^{-11} \text{ cm}^2$ . These values were chosen in agreement with previous literature reports [12, 35–37].

In figure 6 the band diagram at the equilibrium of the simulated structure is reported. The hole tunneling has been implemented from the interface between the EBL and the undoped spacer (blue line). The electron tunneling, instead, can start from the n-type side, from the interface between the n-doped barrier and spacer (red line). The length of the region along which tunneling can take place is equal to the distance between the two interfaces (38 nm).

In the diagram the superlattice underlayer can be noticed. It includes AlInN layers with energy gap equal to 5.17 eV alternating with GaN [34, 38, 45]. These layers do not obstruct the path of electrons, owing to the very low thickness. For each of these ‘barriers’ tunneling was implemented using the Wentzel-Kramers-Brillouin Tunneling Probability model, as described in [17].

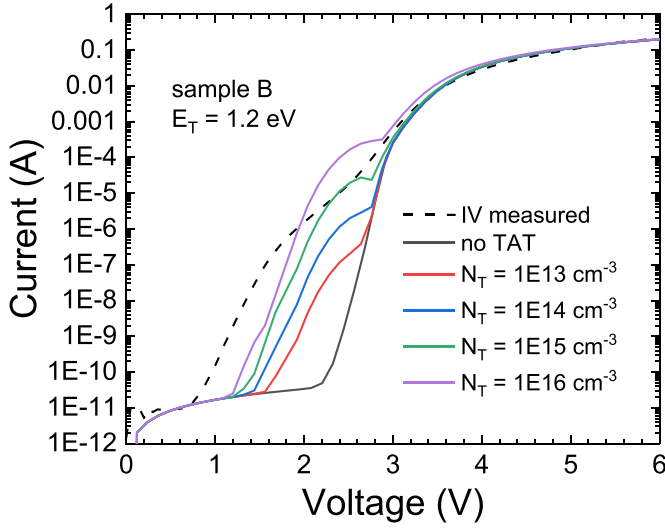


**Figure 7.** Sub-threshold current variations due to the TAT as the concentration of traps  $N_T$  increases and the other parameters remain constant. If the concentration  $N_T$  raises the tunnel probability increases.

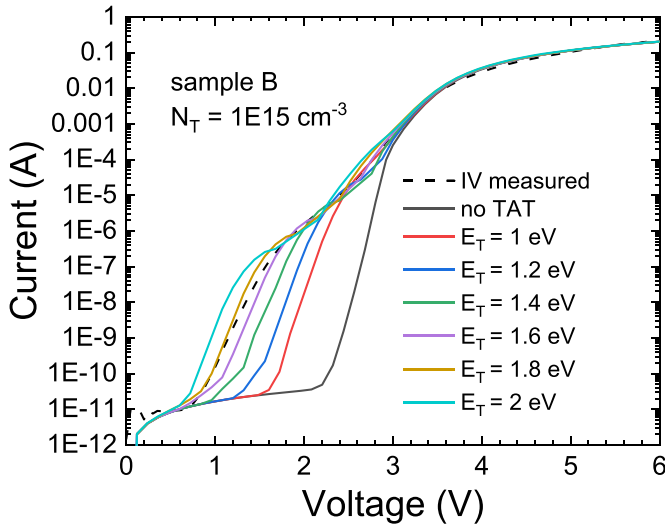


**Figure 8.** Sub-threshold current variations due to the TAT as the energy level of traps  $E_T$  increases and the other parameters remain constant. The variation of  $E_T$  modify the tunneling path length between the trap states and the free carriers changing the tunneling probability.

## 5. Parameter calibration

After setting up the model for TAT, we evaluated the sensitivity of the model to the main parameters, including energy level and concentration of the traps responsible for TAT. The results are summarized in figures 7 and 8. As can be noticed in figures, TAT is a dominant mechanism at low currents; it strongly impacts on conduction below the turn-on voltage, and depends on the presence of defects in the AR.

A parametric analysis was carried out for the sample B. Similar results were obtained for the other samples. The energy level  $E_T$  has been kept constant at 1.2 eV and the

**Table 4.** Most significant simulation parameters. Note that the activation energies and concentrations of defects are exactly those obtained from the deep-level optical spectroscopy and Light-Dark CVs. ( $R_s$  = Series resistance;  $R_p$  = parallel resistance;  $m_{t,e}$  and  $m_{t,h}$  = relative tunneling mass for electrons and holes;  $E_T$  and  $N_T$  = the defect energy level and its concentration;  $\sigma$  = the Gaussian energy distribution;  $E_{wk}$  = the work function of platinum and PE = the activation percentage of piezoelectric polarization.).

sample	A (1.3 nm)	B (1.8 nm)	C (2.4 nm)
$R_s$ ( $\Omega$ )	9	10	12
$R_p$ ( $\Omega$ )	6E10	6E10	6E10
$m_{t,e}$	0.007	0.007	0.007
$m_{t,h}$	0.5	0.5	0.5
$E_C - E_{T,1}$ (eV)	1.29	1.28	1.29
$N_{T,1}$ ( $\text{cm}^{-3}$ )	7.66E14	1.57E15	4.85E15
$E_C - E_{T,2}$ (eV)	1.71	1.72	1.67
$N_{T,2}$ ( $\text{cm}^{-3}$ )	1.276E15	1.23E15	3.21E15
$\sigma_1$ (meV)	5	5	5
$\sigma_2$ (meV)	5	5	5
$E_{wk}$ (eV)	6.35	6.35	6.35
PE	0.65	0.65	0.65

concentration of traps  $N_T$  was varied. For simplicity, it is assumed that the traps are all placed at a single energy level, with a narrow Gaussian energy distribution, having  $\sigma = 5$  meV. In figure 7 an increase in tunneling can be observed with increasing concentration of the traps. This is in line with expectations, since an increase in the amount of traps increases the probability of tunneling (equation (2)). No significant differences were observed in whether the traps were acceptors or donors.

A second simulation was performed by keeping  $N_T$  constant at  $1 \times 10^{15} \text{ cm}^{-3}$ , but now varying the energy level of the traps  $E_T$  (figure 8). By varying  $E_T$ , a variation of the onset voltage of the tunneling process can be observed. In this case we have a reduction of the tunneling onset voltage when  $E_T$  approaches the valence band  $E_V$ . This result is explained by considering the variation in the forward voltage that should be applied so that the level of the traps is energetically aligned with the conduction band of the starting interface of the electrons. Therefore, a lower voltage may be needed to obtain relatively high tunneling probabilities.

As a final step, to model the results obtained experimentally, the traps have been placed in the two levels identified in the SSPC measurements with the concentrations obtained from the Light-Dark CVs. The values of the parameters used for the simulations are reported in the table 4. The activation energies and concentrations of defects are exactly those obtained from the deep-level optical spectroscopy and Light-Dark CVs.

## 6. Simulation results

Figure 9 shows the results of the  $IV$  simulations with the parameters listed above. The results indicate that the concentrations and activation energies obtained from SSPC and LCV measurements can directly be fed into the simulator,

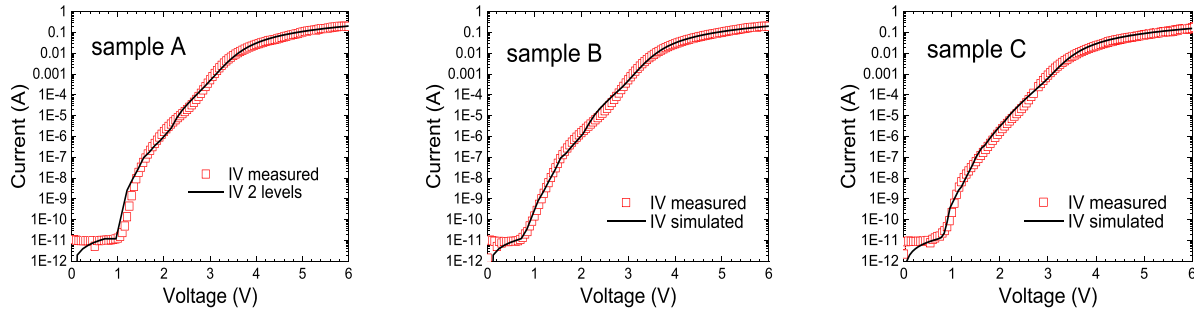


**Figure 9.** Comparison between the experimental electrical characteristics (red symbols) and the simulated ones (black lines) for the three samples.

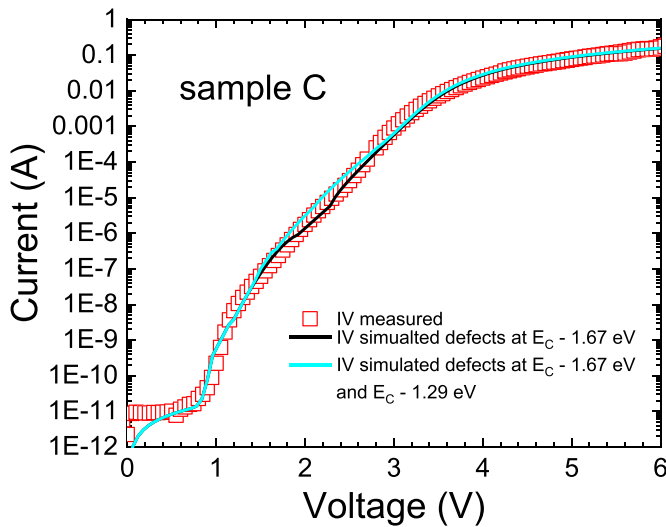


**Figure 10.** Comparison between the electric characteristic with the presence of two energy levels at 1.29 eV and 1.67 eV in the undoped spacer (previous simulation) and with the presence of only a level at 1.67 eV as reported by Armstrong *et al* [19].

and permit to accurately reproduce the current–voltage characteristics of the devices. It is worth noticing that the second level, with activation energy about 1.7 eV from the conduction band and with the same experimental concentrations, influences tunneling at lower voltages compared to the first level (1.28 eV), for which the tunneling probability is smaller. This is in agreement with previous papers, that suggested that states near midgap, like the detected 1.7 eV level, have a higher TAT probability in LEDs [1, 3–6, 10]. The matching obtained over ten order of magnitude of current confirms that the sub-turn on current is mainly given by TAT, and that it depends on the deep defects located in the AR.

It is important to highlight that the SSPC measurements performed in this paper do not allow to discriminate in which layer the traps are spatially located, since the width of the depleted region includes both InGaN and GaN layer. For this reason, in the simulation we placed the two defects in both InGaN and GaN layers near the junction.

Additional comments can be made by looking at the literature: by reading Armstrong *et al* [19], one can see that the defect exhibiting an optical activation energy of 2.11 eV

( $E_T = 1.67\text{--}1.72$  eV) has been associated to the GaN layers, whereas the defect with  $E_a = 1.62$  eV ( $E_T = 1.28\text{--}1.29$  eV) has been related to the QW. This experimental behavior is compatible with the possible decrease in activation energy for defects located in layers with narrower energy gap [39]. Similar results have been reported also in [20, 40]. Our results showed that also with this defect distribution, the simulations can still provide a good matching. This is due to the fact that TAT takes place in the undoped spacer and depends mainly on the deeper level, whose placement remains unchanged. A comparison between the two defect configurations is reported in figure 10, where the contribution of the less deep level is evident to be at higher voltage (1.8 – 3 V).

A final observation concerns the relatively small value of the tunneling mass adopted for the electrons that originates from the complexity of the real physical process. In the case of simple direct tunneling the effective tunneling mass can be obtained with a reasonable accuracy, but already in the case of a single trap-assisted-tunneling the values can differ [10, 41, 42], due to the difference between the real lattice configuration and the one assumed by the simulator model. The situation becomes even more complicated when we move to a possible trap-to-trap tunneling process, where the potential profile and the lattice configuration coordinate is hard to evaluate. For this reason, no simulator provides an effective model for trap-to-trap tunneling, and its consequent non-ideality is modeled as a low effective tunneling mass [43–45], accounting for the trap-to-trap interactions not included in the model.

These results have at least two important implications: (a) the study of current–voltage characteristics in log-scale can provide relevant information on the presence of defects within the AR of LEDs; specifically, from the analysis of the  $I$ – $V$  curves it is possible to identify the presence and contribution of defects near midgap, that are also responsible for SRH recombination [2–4]. The combination of a simple log-scaled  $I$ – $V$  plot and a suitable model can be used to get important information on semiconductor quality. (b) Previous reports indicated that during LED ageing the sub-turn on current components may increase, due to the generation/propagation defects through the AR of the devices [7–9]. The model studied within this paper allows to reproduce changes in the density of traps, and the related impact on the current–voltage characteristics, thus allowing an effective study of the effects of ageing on the characteristics of the devices.



## 7. Conclusions

In this paper we have analyzed and modeled the impact of defects on the electrical characteristic of single QW InGaN/GaN LEDs. In the first experimental phase, thanks to SSPC, two main levels have been identified for traps located near/within the AR (1.28–1.29 eV and 1.67–1.72 eV from  $E_C$ ). LCV measurements were then carried out, to compute the concentrations of defects in the AR of the devices. We showed that the amount of defects increases with the thickness of the QW, confirming the fact that the defects are preferably incorporated in In-containing layers.

Subsequently we proposed a model capable of emulating the electrical behavior of the devices. We demonstrated that the deep states identified experimentally are responsible for TAT processes, that significantly increase the sub turn-on leakage current. A good correspondence was obtained between the simulated and experimental  $I$ – $V$  curves (for over ten orders of magnitude), by using the defect energy and concentration values obtained experimentally as simulation parameters.

The powerful approach defined within this paper can be effectively used to assess the presence of defects within QW LEDs, based on the combination of optical spectroscopy measurements and current–voltage simulations. The same approach can be used also to evaluate the generation of defects during long-term ageing tests.

## Data availability statement

The data that support the findings of this study are available upon reasonable request from the authors.

## Acknowledgments

This research was partly performed within the project INTERNET OF THINGS: SVILUPPI METODOLOGICI, TECNOLOGICI E APPLICATIVI, co-founded (2018–2022) by the Italian Ministry of Education, Universities and Research (MIUR) under the aegis of the ‘Fondo per il finanziamento dei dipartimenti universitari di eccellenza’ initiative (Law 232/2016).

## ORCID iDs

Nicola Roccatto  <https://orcid.org/0000-0002-6762-6695>  
 Francesco Piva  <https://orcid.org/0000-0003-3620-5510>  
 Marco Vallone  <https://orcid.org/0000-0003-3392-1810>  
 Alberto Tibaldi  <https://orcid.org/0000-0002-0157-8512>  
 Gaudenzio Meneghesso  <https://orcid.org/0000-0002-6715-4827>

## References

- [1] Verzellesi G, Saguatti D, Meneghini M, Bertazzi F, Goano M, Meneghesso G and Zanoni E 2013 Efficiency droop in InGaN/GaN blue light-emitting diodes: physical mechanisms and remedies *J. Appl. Phys.* **114** 71101
- [2] Chichibu S F, Uedono A, Kojima K, Ikeda H, Fujito K, Takashima S, Edo M, Ueno K and Ishibashi S 2018 The origins and properties of intrinsic nonradiative recombination centers in wide bandgap GaN and AlGaIn *J. Appl. Phys.* **123** 161413
- [3] Langer T, Jönen H, Kruse A, Bremers H, Rossow U and Hangleiter A 2013 Strain-induced defects as nonradiative recombination centers in green-emitting GaInN/GaN quantum well structures *Appl. Phys. Lett.* **103** 022108
- [4] Bochkareva N I, Voronenkov V V, Gorbunov R I, Zubrilov A S, Lelikov Y S, Latyshev P E, Rebane Y T, Tsyuk A I and Shreter Y G 2010 Defect-related tunneling mechanism of efficiency droop in III-nitride light-emitting diodes *Appl. Phys. Lett.* **96** 133502
- [5] Han D P, Zheng D G, Oh C H, Kim H, Shim J I, Shin D S and Kim K S 2014 Nonradiative recombination mechanisms in InGaN/GaN-based light-emitting diodes investigated by temperature-dependent measurements *Appl. Phys. Lett.* **104** 151108
- [6] De Santi C, Buffolo M, Renso N, Neviani A, Meneghesso G, Zanoni E and Meneghini M 2019 Evidence for defect-assisted tunneling and recombination at extremely low current in InGaN/GaN-based LEDs *Appl. Phys. Express* **12** 052007
- [7] Liu J, Wong H, Siu S L, Kok C W and Filip V 2012 Degradation behaviors of GaN light-emitting diodes under high-temperature and high-current stressing *Microelectron. Reliab.* **52** 1636–9
- [8] Cao X A, Sandvik P M, LeBoeuf S F and Arthur S D 2003 Defect generation in InGaN/GaN light-emitting diodes under forward and reverse electrical stresses *Microelectron. Reliab.* **43** 1987–91
- [9] Chuang S L, Ishibashi A, Kijima S, Nakayama N, Ukita M and Taniguchi S 1997 Kinetic model for degradation of light-emitting diodes *IEEE J. Quantum Electron.* **33** 970–9
- [10] Auf Der Maur M, Galler B, Pietzonka I, Strassburg M, Lugauer H and Di Carlo A 2014 Trap-assisted tunneling in InGaN/GaN single-quantum-well light-emitting diodes *Appl. Phys. Lett.* **105** 133504
- [11] Bertazzi F et al 2015 Modeling challenges for high-efficiency visible light-emitting diodes 2015 *IEEE 1st Int. Forum on Research and Technologies for Society and Industry, RTSI 2015—Proc. (November)* pp 157–60
- [12] Mandurino M, Verzellesi G, Goano M, Vallone M, Bertazzi F, Ghione G, Meneghini M, Meneghesso G and Zanoni E 2015 Physics-based modeling and experimental implications of trap-assisted tunneling in InGaN/GaN light-emitting diodes *Phys. Status Solidi* **212** 947–53
- [13] Piva F et al 2020 Defect incorporation in In-containing layers and quantum wells: experimental analysis via deep level profiling and optical spectroscopy *J. Appl. Phys.* **54** 7
- [14] Haller C, Carlin J F, Jacopin G, Martin D, Butté R and Grandjean N 2017 Burying non-radiative defects in InGaN underlayer to increase InGaN/GaN quantum well efficiency *Appl. Phys. Lett.* **111** 262101
- [15] Haller C, Carlin J F, Jacopin G, Liu W, Martin D, Butté R and Grandjean N 2018 GaN surface as the source of non-radiative defects in InGaN/GaN quantum wells *Appl. Phys. Lett.* **113** 111106
- [16] Polyakov A Y et al 2019 Effects of InAlN underlayer on deep traps detected in near-UV InGaN/GaN single quantum well light-emitting diodes *J. Appl. Phys.* **126** 125708
- [17] Synopsys and Inc 2015 Sentaurus™ device user guide (available at: [www.synopsys.com/Company/Pages/Trademarks.aspx](http://www.synopsys.com/Company/Pages/Trademarks.aspx)) (Accessed 02 August 2020)
- [18] Synopsys and Inc 2015 Sentaurus™ structure editor user guide destination control statement (available at: [www.synopsys.com/Company/Pages/Trademarks.aspx](http://www.synopsys.com/Company/Pages/Trademarks.aspx)) (Accessed 30 July 2020)

- [19] Armstrong A, Henry T A, Koleske D D, Crawford M H and Lee S R 2012 Quantitative and depth-resolved deep level defect distributions in InGaN/GaN light emitting diodes *Opt. Express* **20** A812
- [20] Armstrong A M, Bryant B N, Crawford M H, Koleske D D, Lee S R and Wierer J J 2015 Defect-reduction mechanism for improving radiative efficiency in InGaN/GaN light-emitting diodes using InGaN underlayers *J. Appl. Phys.* **117** 134501
- [21] Armstrong A M, Crawford M H and Koleske D D 2014 Contribution of deep-level defects to decreasing radiative efficiency of InGaN/GaN quantum wells with increasing emission wavelength *Appl. Phys. Express* **7** 032101
- [22] Pässler R 2004 Photoionization cross-section analysis for a deep trap contributing to current collapse in GaN field-effect transistors *J. Appl. Phys.* **96** 715–22
- [23] Cho H K, Lee J Y, Kim C S and Yang G M 2002 Influence of strain relaxation on structural and optical characteristics of InGaN/GaN multiple quantum wells with high indium composition *J. Appl. Phys.* **91** 1166–70
- [24] Wang H, Jiang D S, Jahn U, Zhu J J, Zhao D G, Liu Z S, Zhang S M, Qiu Y X and Yang H 2010 Investigation on the strain relaxation of InGaN layer and its effects on the InGaN structural and optical properties *Phys. B* **405** 4668–72
- [25] Ploch S, Wernicke T, Frentrup M, Pristovsek M, Weyers M and Kneissl M 2012 Indium incorporation efficiency and critical layer thickness of (2021) InGaN layers on GaN *Appl. Phys. Lett.* **101** 202102
- [26] Götz W, Johnson N M, Chen C, Liu H, Kuo C and Imler W 1996 Activation energies of Si donors in GaN *Appl. Phys. Lett.* **68** 3144–6
- [27] Zhao C Z, Wei T, Chen L Y, Wang S S and Wang J 2017 The activation energy for Mg acceptor in Al<sub>x</sub>Ga<sub>1-x</sub>N alloys in the whole composition range *Superlattices Microstruct.* **109** 758–62
- [28] Nakano Y and Jimbo T 2002 Electrical properties of acceptor levels in Mg-Doped GaN *Phys. Status Solidi* **1** 438–42
- [29] Silvestri L, Dunn K, Prawer S and Ladouceur F 2011 Hybrid functional study of Si and O donors in wurtzite AlN *Appl. Phys. Lett.* **99** 122109
- [30] Averkiev N S, Chernyakov A E, Levinshtein M E, Petrov P V, Yakimov E B, Shmidt N M and Shabunina E I 2009 Two channels of non-radiative recombination in InGaN/GaN LEDs *Phys. B* **404** 4896–8
- [31] Michaelson H B 1977 The work function of the elements and its periodicity related articles the work function of the elements and its periodicity *Cit. J. Appl. Phys.* **48** 4729
- [32] Lin Y J 2006 Comment on ‘contact mechanisms and design principles for alloyed ohmic contacts to n-GaN’ [*J. Appl. Phys.* 95, 7940 (2004)] *J. Appl. Phys.* **100** 073707
- [33] Mandurrino M 2013 Politecnico di torino laurea specialistica in ingegneria fisica TCAD models for tunneling processes in narrow-gap semiconductors
- [34] Jiménez-Molinos F, Gámiz F, Palma A, Cartujo P and López-Villanueva J A 2002 Direct and trap-assisted elastic tunneling through ultrathin gate oxides *J. Appl. Phys.* **91** 5116–24
- [35] Levinshtein M, Rumyantsev S L and Shur M S 2001 *Properties of Advanced Semiconductor Materials: GaN, AlN, InN, BN, SiC, SiGe* (New York: Wiley)
- [36] Alkauskas A, McCluskey M D and Van De Walle C G 2016 Tutorial: defects in semiconductors—combining experiment and theory *J. Appl. Phys.* **119** 181101
- [37] Mandurrino M, Goano M, Vallone M, Bertazzi F, Ghione G, Verzellesi G, Meneghini M, Meneghesso G and Zanoni E 2015 Semiclassical simulation of trap-assisted tunneling in GaN-based light-emitting diodes *J. Comput. Electron.* **14** 444–55
- [38] Pelá R R, Caetano C, Marques M, Ferreira L G, Furthmüller J and Teles L K 2011 Accurate band gaps of AlGa<sub>x</sub>N, InGa<sub>x</sub>N, and AlIn<sub>x</sub>N alloys calculations based on LDA-1/2 approach *Appl. Phys. Lett.* **98** 151907
- [39] Wickramaratne D, Dreyer C E, Shen J X, Lyons J L, Alkauskas A and Van De Walle C G 2020 Deep-level defects and impurities in InGa<sub>x</sub>N alloys *Phys. Status Solidi Basic Res.* **257** 1900534
- [40] Armstrong A, Henry T A, Koleske D D, Crawford M H, Westlake K R and Lee S R 2012 Dependence of radiative efficiency and deep level defect incorporation on threading dislocation density for InGa<sub>x</sub>N/GaN light emitting diodes *Appl. Phys. Lett.* **101** 162102
- [41] Schenk A and Heiser G 1998 Modeling and simulation of tunneling through ultra-thin gate dielectrics *J. Appl. Phys.* **81** 7900
- [42] Schenk A 1993 Rigorous theory and simplified model of the band-to-band tunneling in silicon *Solid. State. Electron.* **36** 19–34
- [43] Miller E J, Yu E T, Waltereit P and Speck J S 2004 Analysis of reverse-bias leakage current mechanisms in GaN grown by molecular-beam epitaxy *Appl. Phys. Lett.* **84** 535
- [44] Gonzalez M B, Eneman G, Wang G, De Jaeger B, Simoen E and Claeys C 2011 Analysis of the temperature dependence of trap-assisted tunneling in Ge pFET junctions *J. Electrochem. Soc.* **158** H955
- [45] Zhang H, Miller E J and Yu E T 2006 Analysis of leakage current mechanisms in Schottky contacts to GaN and Al<sub>0.25</sub>Ga<sub>0.75</sub>N/GaN grown by molecular-beam epitaxy *J. Appl. Phys.* **99** 023703